Developmental Cell
Article

PTEN Controls Junction Lengthening and Stability during Cell Rearrangement in Epithelial Tissue

Pierre-Luc Bardet,[1,3] Boris Guirao,[1,3] Camille Paoletti,[1,4] Fanny Serman,[1] Valentine Léopold,[1] Floris Bosveld,[1] Yûki Goya,[1] Vincent Mirouse,[2] François Graner,[1,5] and Yohanns Bellaïche[1,*]

[1]Polarity Division and Morphogenesis Team, Institut Curie, CNRS UMR 3215, INSERM U934, 26 rue d'Ulm, 75248 Paris Cedex 05, France
[2]GReD, CNRS UMR 6293, INSERM U1103, Clermont Université 28, Place Henri Dunant, 63000 Clermont-Ferrand, France
[3]These authors contributed equally to this work
[4]Present address: Institut de Biologie Moléculaire et Cellulaire, 1 rue Laurent Fries, 67400 Illkirch Cedex, France
[5]Present address: Matière et Systèmes Complexes, CNRS UMR 7057, Université Paris Diderot, 10 rue Alice Domon et Léonie Duquet, 75205 Paris Cedex 13, France
*Correspondence: yohanns.bellaiche@curie.fr
http://dx.doi.org/10.1016/j.devcel.2013.04.020

SUMMARY

Planar cell rearrangements control epithelial tissue morphogenesis and cellular pattern formation. They lead to the formation of new junctions whose length and stability determine the cellular pattern of tissues. Here, we show that during *Drosophila* wing development the loss of the tumor suppressor PTEN disrupts cell rearrangements by preventing the lengthening of newly formed junctions that become unstable and keep on rearranging. We demonstrate that the failure to lengthen and to stabilize is caused by the lack of a decrease of Myosin II and Rho-kinase concentration at the newly formed junctions. This defect results in a heterogeneous cortical contractility at cell junctions that disrupts regular hexagonal pattern formation. By identifying PTEN as a specific regulator of junction lengthening and stability, our results uncover how a homogenous distribution of cortical contractility along the cell cortex is restored during cell rearrangement to control the formation of epithelial cellular pattern.

INTRODUCTION

Planar cell rearrangements play a fundamental role in epithelial tissue morphogenesis as they allow the remodeling of tissues while maintaining their cohesiveness. They occur by E-cadherin (E-Cad) adherens junction (AJ) remodeling: cell junctions shorten, bringing four or more cells in contact; after neighbor exchange, new junctions regrow, roughly orthogonal to the previous ones (Keller, 2006). Cell rearrangement thus locally affects cell shape and topology and has been recognized as a major epithelial remodeling process both in invertebrate and vertebrates (Keller, 2006). So far, most studies have focused on the mechanisms of junction shortening that have been extensively studied during the gastrulation of the *Drosophila* embryo (for review, see Lecuit et al., 2011). They rely on the local increase of cortical contractility associated with the dynamic accumulation of myosin II (MyoII) at shortening junctions (Bertet et al., 2004; Nishimura et al., 2012; Rauzi et al., 2010; de Matos Simões et al., 2010; Zallen and Wieschaus, 2004). However, little is known about the mechanisms controlling the lengthening and the stabilization of newly formed junctions in developing tissues.

The length and the stability of junctions are critical to the spatial organization of cells in the epithelium (cell packing, McKenzie et al., 2004; Narimatsu et al., 2009; Nowak et al., 2009; Togashi et al., 2011). Numerous tissues are mostly composed of regular hexagonal cells characterized by AJs of similar lengths (Classen et al., 2005; Gibson et al., 2006; Narimatsu et al., 2009; Tardieu, 1988). At steady state, junction lengths are proposed to be dependent on E-Cad-mediated adhesion, which expands cell-cell contacts, and on MyoII-dependent cortical contractility, which reduces cell junction and perimeters (Lecuit and Lenne, 2007; Maître et al., 2012). Accordingly, quantitative models have analyzed how the adhesion/contractility balance determines junction length, junction tension, and epithelial cell packing (Aigouy et al., 2010; Farhadifar et al., 2007; Graner and Sawada, 1993; Hilgenfeldt et al., 2008; Käfer et al., 2007; Rauzi et al., 2008; Staple et al., 2010). In such models, the regular hexagonal packing corresponds to an energy minimum when all cells have the same physical properties and a homogenous distribution of adhesiveness and contractility on their junctions (Farhadifar et al., 2007; Staple et al., 2010). Although the small GTPase Rap1 is a regulator of E-Cad homogenous distribution in *Drosophila* epithelial cells (Knox and Brown, 2002), the mechanisms promoting a homogenous cortical distribution of MyoII at cell junctions are so far not characterized.

During *Drosophila* pupal wing development, cell rearrangements are concomitant to tissue elongation and hexagonal packing formation (Aigouy et al., 2010). The contraction of the proximal wing hinge region triggers wing blade elongation and oriented cell rearrangements resulting in a tissue with an elongated shape and regular cell packing at the end of morphogenesis, reminiscent of a honeycomb (Aigouy et al., 2010; Classen et al., 2005). This honeycomb-like pattern formation depends on the activity of the Fat/Dachsous and Frizzled planar cell polarity pathways, both of which regulate cell rearrangements (Aigouy et al., 2010; Bosveld et al., 2012; Classen et al., 2005; Harumoto et al., 2010; Ma et al., 2008; Warrington et al., 2013). We

therefore explored whether genes whose loss of function disrupts the final honeycomb packing might be involved in de novo junction formation or elongation during cell rearrangement. Because in vitro studies have shown that formation of new junctions is associated with the activation of the phosphatidylinositol-4,5-bisphosphate 3-kinase (PI3K), whose role in this process remains poorly understood (see discussion in Yamada and Nelson, 2007), we analyzed whether the phosphatidylinositol cycle enzymes control the wing hexagonal cell packing.

Here we characterized how the tumor suppressor PTEN (phosphatase and tensin homolog on chromosome 10) regulates cell packing in the wing. PTEN is frequently inactivated in a wide range of human sporadic tumors (for review, see Chalhoub and Baker, 2009). PTEN is a lipid phosphatase, and its major function is to dephosphorylate phosphatidylinositol (3,4,5)-triphosphate (PIP3) to produce phosphatidylinositol (4,5)-bisphosphate (PIP2). This influences the membrane localization and activation of several key proteins involved in growth control (Chalhoub and Baker, 2009). In epithelia, PTEN participates in cell polarization in conjunction with the Par complex proteins (Martin-Belmonte et al., 2007; Pickering et al., 2013; Pinal et al., 2006), and in cell packing by yet uncharacterized mechanisms (Ma et al., 2008). By combining real-time imaging in *Drosophila* wing epithelium with physical modeling and numerical simulations, we identified PTEN as an essential regulator of junction mechanical properties, which in turn control their lengthening and stability during cell rearrangements. Furthermore our work uncovers an unexpected connection between junction elongation and restoration of a homogenous cortical tensile stress distribution at cell junction, thereby controlling the final epithelial cell packing.

RESULTS

PTEN Loss of Function Gives Rise to Cobblestone and Rosette Packing Characterized by an Excess of Short Junctions

From 28–30 hr after pupa formation (hAPF) onward, *Drosophila* wing intervein epithelium exhibits regular hexagonal cell packing with 75% of cells being six-sided (Classen et al., 2005 and this study) (Figures 1A–1D). Knocking down the phosphatidylinositol cycle enzymes genes (P-L.B., V.L., F.G., and Y.B., unpublished data), we observed that, as previously reported (Ma et al., 2008), the loss of PIP3 phosphatase PTEN function disrupts intervein epithelium cell packing (Figures 1A and 1B). We found that in *pten* tissue, only 50% of the cells were six-sided (Figures 1C and 1D). Furthermore, the tissue exhibits cell patterns with distinctive local cobblestone patterns and some rosette patterns (Figure 1B). The *pten* packing is characterized by a mixing of short and long cell junctions (Figure 1E) that can be quantified by the distribution of junction lengths in the tissue and by the mean heterogeneity of junction lengths for each cell. In the wild-type (WT) tissue, most cell shapes were close to regular hexagons (“honeycomb-like”) and their side length distribution exhibited a single peak (Figure 1F). Instead, *pten* side length distribution was bimodal, with an excess of short sides ($p < 10^{-10}$) (Figures 1E and 1F). Moreover, side length heterogeneity was significantly higher in *pten* cells than in WT cells ($p < 10^{-10}$) (Figures 1G and 1H). Comparable distributions were observed with two *pten* null alleles or in cells expressing a *pten* dsRNA ($pten^{RNAi}$) (Figures 1F and 1H). PTEN antagonizes the activity of PI3K (Chalhoub and Baker, 2009). Accordingly, overexpression of the PI3K catalytic subunit recapitulated the *pten* phenotype (Figures S1A and S1B available online).

Known deleterious effects of PTEN loss of function in *Drosophila* epithelial tissue including overgrowth and apical-basal polarization defects depend on Akt function (Pinal et al., 2006; Stocker et al., 2002). Our following findings exclude that the *pten* packing phenotype is a consequence of a role of PTEN in cell growth: (1) loss of *akt* function, which rescues the *pten* overgrowth phenotype (Stocker et al., 2002), does not rescue the *pten* packing phenotype (Figures S1C–S1G), (2) the apical area of *pten* cells is identical to the one of wild-type cells between 20 and 30 hAPF (Figures S1H–S1K′), and (3) whereas the overexpression of *rheb* produces a wing overgrowth phenotype similar to the one observed upon PTEN loss of function, the overexpression of *rheb* does not affect hexagonal cell packing (Figures S1L–S1Q). Furthermore the *pten* phenotype is not a consequence of a loss of apical-basal polarization: although some polarity protein levels were slightly more elevated in *pten* tissue, neither apical markers (E-cad, Crumbs, Par3/Bazooka) nor basal ones (Fasciclin III, Discs-large) were shifted along the apical-basal axis (Figures S1R–S1W′). Accordingly, Par3/Bazooka, a regulator of PTEN localization, does not control cell packing and its loss of function does not suppress the *pten* phenotype (Figures S1X–S1Z). Together, our results suggest the existence of an additional mechanism of action of PTEN in epithelial tissue organization.

Heterogeneous Distribution of Junction Tension Can Account for Local Cobblestone Patterns Observed in *pten* Tissue

Theoretical models have analyzed how the adhesion/contractility balance determines epithelial cell packing (Aigouy et al., 2010; Farhadifar et al., 2007; Graner and Sawada, 1993; Hilgenfeldt et al., 2008; Käfer et al., 2007; Maître et al., 2012; Rauzi et al., 2008). We therefore explored whether and how the modulation of the adhesion/contractility balance at each junction can generate the cell junction length heterogeneity observed in *pten* tissue. To this end, we developed an analytical cell shape model where the adhesion/contractility balance at each side is modeled by the dimensionless “side parameter” λ (see the Supplemental Experimental Procedures). Lambda increases with adhesion and decreases with contractility, and can either be the same at all sides (homogenous), or vary from side to side (heterogeneous).

Considering a periodic cellular lattice to keep the model analytically tractable (Figure 2A, inset), each normalized side tension γ then depends on its side parameter and on the cell normalized perimeter (p): $\gamma = p - \lambda$. First, we determined that when all sides have the same side parameter value and contractility dominates adhesion ($\lambda = \lambda_o$ with $0 < \lambda_o < p_H$, where $p_H \approx 3.72$ is the normalized perimeter of the regular hexagon), the lattice adopts a honeycomb organization comparable to WT tissue (Aigouy et al., 2010; Farhadifar et al., 2007), with p reaching its minimal value p_H (Hales, 2001), homogenous side length l and tension $\gamma > 0$ (Figures 2A and S2A). Then, we found two mutually exclusive hypotheses both leading to cobblestone patterns, namely hexagons with two sides much shorter than the others,

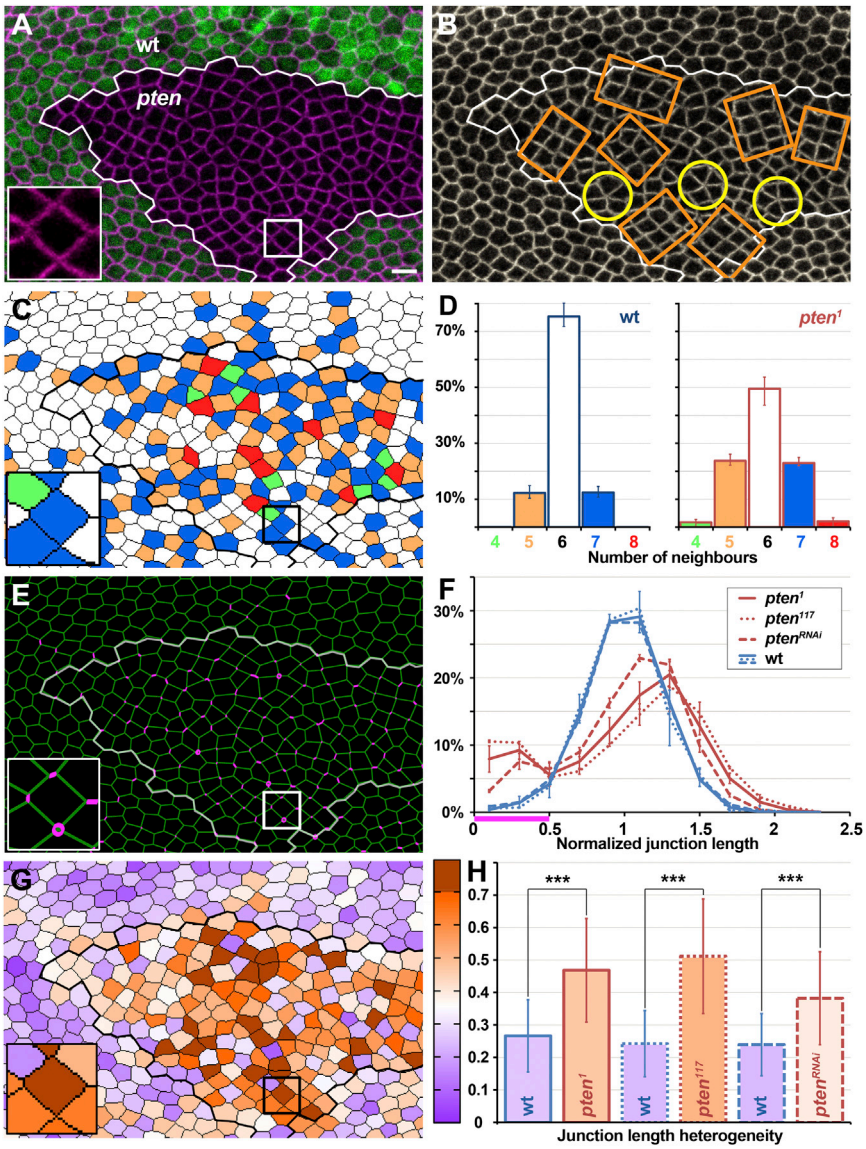

Figure 1. Loss of *pten* Leads to Cell Junction Length Heterogeneity at 30 hAPF

(A–C) A clone of *pten*^{1} cells marked by the absence of GFP (green in A; clone boundary is depicted by a white line in A and B) in an otherwise control pupal wing intervein tissue. E-cad staining outlines cell apical junctions (magenta in A; gray in B), and was skeletonized to obtain (C, clone boundary is depicted by a black line). In (B) some cobblestone (orange frames) and rosette patterns (yellow circles) are highlighted. A typical cell within a cobblestone pattern (frame in A and C) is enlarged in inset in (A) and (C). Number of neighbors of each cell is represented by a color in C (4, green; 5, orange; 6, white; 7, blue and 8, red).

(D) Histogram of the number of cell neighbors in WT (left) and *pten*^{1} (right) tissue. Bars indicate the SD of distributions.

(E) The tissue region shown in (A) was skeletonized to obtain (E). The *pten* clone boundary is depicted by a white line. Short sides (<0.5 × average length) are shown in magenta and with magenta circles indicating 4-fold vertices. A typical cell within a cobblestone pattern (frame) is enlarged in inset in (E).

(F) Histogram of the junction length distributions in *pten*^{1}, *pten*^{117}, and *pten*^{RNAi} and their corresponding WT controls. Junction lengths are normalized by the average length. Bars indicate the SD of distributions.

(G) The tissue region shown in (A) was skeletonized to obtain (G). The *pten* clone boundary is depicted by a black line. The junction length heterogeneity per cell is represented by colors, ranging from dark purple (homogeneous, close to 0) to dark orange (very heterogeneous, close to 1). A typical cell within a cobblestone pattern (frame) is enlarged in inset in (G).

(H) Graph of junction length heterogeneity average in *pten*^{1}, *pten*^{117}, and *pten*^{RNAi} and their corresponding WT control tissues. Colored bars indicate the SD of distributions and stars indicate statistical significance (***$p < 10^{-10}$).

Quantifications for (D), (F), and (H) were performed on: *pten*^{1}: eight clones in three wings, 1,736 cells, 4,329 sides; WT control: 2,654 cells, 6,955 sides; *pten*^{117}: two clones in two wings, 665 cells, 1,829 sides. WT: 509 cells, 1,325 sides; *pten*^{RNAi}: two wings (posterior compartment), 3,291 cells, 9,228 sides; WT: same wings (anterior compartment), 1,262 cells, 3,460 sides. Scale bar represents 5 μm. See also Figure S1.

as observed in parts of *pten* wings (Figure 2B). (1) The "homogeneous and $\gamma = 0$" hypothesis (case 1 in Figures 2, S2B, and S2C): all sides have the same side parameter value and adhesion dominates contractility ($\lambda = \lambda_o$ and $\lambda_o > p_H$); these cobblestone patterns are characterized by vanishing side tensions ($\gamma = 0$). (2) The "heterogeneous and $\gamma > 0$" hypothesis (case 2 in Figures 2B and S2C): cell sides have heterogeneous adhesive/cortical properties, i.e., different λ values; in the model, these cobblestone patterns are characterized by strictly positive side tensions ($\gamma > 0$) that decrease with increasing side length l (Supplemental Experimental Procedures).

To test which of these two hypotheses best describes the *pten* tissue, we probed junction tension γ by measuring the initial relaxation velocity V^o of vertices after laser ablation of single-cell junctions (Figure 2C) (Farhadifar et al., 2007; Hutson et al., 2009; Rauzi et al., 2008). The mean side tension γ was strictly positive and was similar in WT and *pten* cells (Figure 2D). This rules out that the *pten* phenotype is described by the "homogeneous and $\gamma = 0$" hypothesis, but supports the "heterogeneous and $\gamma > 0$" hypothesis. Moreover, side tensions γ decreased with side lengths l (Figure 2D); correlations and linear fits of experimental data of γ versus l were similar in WT and *pten* cells, suggesting that the length-tension relationship is unchanged by PTEN loss of function.

Fitting our model to laser ablation data allowed us to estimate the side parameter mean values as well as their ranges of variation: for the WT, we determined a single value, $\lambda_o \approx 2.3 \pm 0.4$ (Figure S2D); and for *pten*, two values $\lambda_S \approx 1.8 \pm 0.4$, $\lambda_L \approx 2.9 \pm 0.4$ (Figure S2E). The study of the λ-diagram for $0 < \lambda < p_H$ shows that it is made of two complementary

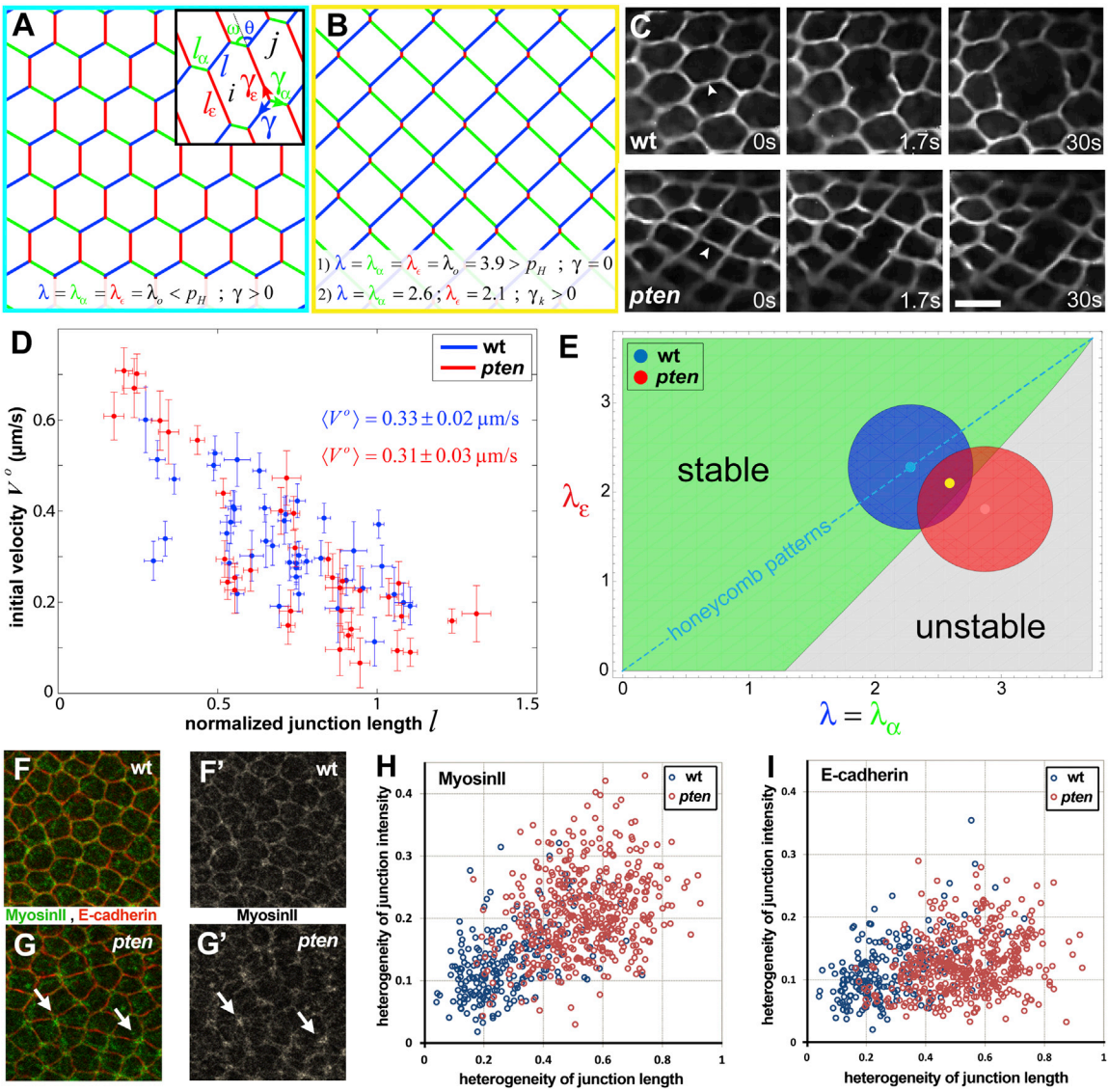

Figure 2. Heterogeneity in Junction Tension Due to Alteration of Adhesion/Contractility Balance Can Account for *pten* Packing

(A) Honeycomb pattern obtained in homogeneous case at any low side parameter value ($\lambda_o < p_H \approx 3.72$). Inset: model notations and cellular lattice. The lattice is made of identical six-sided cells of constant area A_o tiling the plane. Force balance is satisfied at each vertex. A network configuration is fully determined by specification of angles (ω, θ) and dimensionless side lengths $(l, l_\alpha, l_\varepsilon)$. Side length symmetry is broken when these lengths differ.

(B) Cobblestone pattern obtained in either: the "homogeneous and $\gamma = 0$" case at high side parameter value ($\lambda_o = 3.9 > p_H$) or: the "heterogeneous and $\gamma > 0$" case with one side having a side parameter (red, $\lambda_\varepsilon = 2.1$) lower than the other two (green and blue, $\lambda = \lambda_\alpha = 2.6$).

(C) Vertices right before, 1.7 s and 30 s after laser ablation of a single junction (arrowhead) in WT (top) and *pten*[1] cells (bottom).

(D) Junction tension variation with junction length. Initial velocity after ablation V^o (µm/s) is plotted versus dimensionless side length $l = L/\langle A \rangle^{1/2}$, $\langle A \rangle$ being the mean area of intervein cells. Each point corresponds to a cell junction ablation: blue, WT (n = 42); red, *pten*[1] (n = 36). Bars indicate measurement errors on junction length and initial velocity.

(E) Diagram of side parameters in the plane $\lambda = \lambda_\alpha$ for λ in [0, p_H]. The stable domain is colored in green, the unstable one in gray. Domains representing side parameter ranges obtained from laser ablation experiments $[\langle \lambda_k \rangle - 2\sigma_k ; \langle \lambda_k \rangle + 2\sigma_k]$ for WT (blue) and *pten* (red) tissues. The cyan and yellow points correspond to averages of WT domain and of stable part of *pten* domain, respectively, and correspond to patterns shown in (A) and (B). The cyan dashed line represents the set of honeycomb patterns.

(F–G′) Confocal images of WT (F and F′) and *pten*^{RNAi} (G and G′) intervein tissue where MyoII is detected by the localization of MyoII-GFP (green in F and G; gray in F′ and G′) and E-Cad (red in F and G). In *pten*^{RNAi} tissue, MyoII-GFP is heterogeneous and accumulates at the short sides (arrows in G and G′). Note that in wild-type and *pten*^{RNAi} tissues, MyoII-GFP can accumulate as circular or star-shape pattern structures around 4-fold vertex, which represent transient accumulation of MyoII:GFP at both the old and newly-formed junctions.

(H and I) Graph of MyoII (H) and E-cad (I) intensity heterogeneity versus cell junction length heterogeneity in WT (blue dots) and in *pten* (red dots) cells.

Scale bar represents 5 µm. See also Figure S2.

domains: a stable one where hexagonal lattices and all three types of sides can exist and be stable (green region in Figure 2E), and an unstable one where hexagonal lattices cannot exist and where the side with highest tension γ disappears before the energy minimum is reached (gray domain in Figure 2E). We next plotted the domains of this λ-diagram that correspond to the ranges of experimental λ values for WT and *pten* tissues found above (Figure 2E). The WT domain lies almost entirely within the stable domain, thereby adopting a stable honeycomb pattern on average. Conversely, the *pten* domain mostly lies in the unstable domain. This implies that, in *pten*, most parameter values found experimentally involve an unstable side, the shortest one, which shrinks and disappears, possibly leading to a new side that can in turn be stable or not. Importantly, the center of the *pten* stable domain (yellow point) corresponds to a cobblestone pattern (Figure 2B), in agreement with experimental observations.

The analysis of laser ablation experiments with our model predicted that: (1) the heterogeneity of cell junction adhesion/contractility balance can account for the local *pten* cobblestone patterns, and (2) the *pten* phenotype involves instability of most short cell junctions. These two predictions prompted us to perform two complementary analyses. First, we aimed at determining whether the junction length heterogeneity observed in *pten* tissue correlates with defects in the distribution of cadherin and/or MyoII along the cell cortex at 28–30 hAPF. Second, we explored during wing development when and how the short junctions are generated and whether they are indeed unstable.

Heterogeneity of Junction Length Is Associated with a Heterogeneous Distribution of MyoII in *pten* Tissue

To determine whether PTEN leads to heterogeneities in adhesion/contractility, we compared the distributions of E-Cad and of the MyoII regulatory light chain (MyoII) (Royou et al., 2004) along the cortex of WT and *pten* cells. In WT tissue at 28–30 hAPF, the distributions of both E-Cad and MyoII are homogenous around the cell cortex in agreement with the fact that the tissue adopts a honeycomb packing (Figures 2F and 2F′). The distribution of E-Cad remained homogeneous in *pten* cells, whereas the MyoII distribution was remarkably heterogeneous along the cell cortex, being strongly increased on short junctions (Figures 2G and 2G′). Moreover, and in contrast to the E-Cad distribution, we found that the increase in heterogeneity of MyoII intensity positively correlated with the increase in junction length heterogeneity (Figures 2H and 2I). Together these results demonstrate that PTEN affects the distribution of MyoII along the cell cortex. They further suggest that the heterogeneity in MyoII-dependent cortex contractility drives the tension heterogeneity found in *pten* mutant cells.

In *Drosophila* embryo, MyoII is proposed to accumulate at junctions in response to MyoII-dependent tension in adjacent junctions (Fernandez-Gonzalez et al., 2009). This raised the possibility that the PTEN loss of function might induce nonautonomous defects in either cell packing or MyoII localization in cells surrounding the *pten* tissue. Yet, small WT tissue islands surrounding by large *pten* tissue showed a regular packing and normal distribution of MyoII (Figures S2F, S2G, and S2J). In addition, small *pten* clones surrounded by wild-type tissue manifested a packing and a MyoII distribution defects (Figures S2H–S2J). Furthermore, the analysis of junction length distributions at the frontier of WT and *pten* tissues revealed that only the junctions that are common to a *pten* and a WT cell are affected (Figure S2K, purple plain line). Collectively, our results show that loss of PTEN function causes a local defect in cell packing associated with heterogeneous distribution of MyoII localization.

PTEN Loss of Function Causes Cell Rearrangement Defects Where Newly Formed Junctions Fail to Elongate and Become Unstable

In parallel, we imaged a functional E-Cad:GFP (Oda and Tsukita, 2001) in pupal wings expressing a *pten* dsRNA ($pten^{RNAi}$) using the Gal4/Gal80ts system (McGuire et al., 2003) to abrogate PTEN function in the posterior compartment during pupal development. The anterior compartment was used as a WT internal control and its development proceeds in two phases (Aigouy et al., 2010). In a first phase from 20 to 24 hAPF, cells undergo a last round of divisions, rearrange and flow toward the proximal part of the wing. In a second phase from 24 to 30 hAPF, in absence of cell division and flow, cells undergo oriented rearrangements, generating a honeycomb-like packing (Movie S1). In *pten* tissue at 20 hAPF, no major difference with WT tissue was observed, as reflected by the distribution of junction lengths (Figures S3A, S3D, and S3G). From 20 hAPF onward, during and after cell divisions and cell flow, the difference between WT and *pten* tissues became gradually more pronounced leading to the formation of the cobblestone and rosette packing (Figures S3B–S3I; Movie S1). Because cell rearrangement was the only process common to both phases, this prompted us to analyze the dynamics of cell rearrangements in WT and *pten* tissues by tracking individual cell junctions from 23 to 29 hAPF.

In WT and *pten* tissues, the number of junctions that initiated a cell rearrangement was similar (30% in WT, n = 957 and 31% in *pten,* n = 723). Nevertheless, we observed important differences in junction remodeling during cell rearrangements. In WT tissue, when a cell junction shrank and disappeared through a cell rearrangement, it rarely rearranged back and forth more than two additional times (Figures 3A, 3B, and S3L; Movie S2A). In sharp contrast, in *pten* tissue, when a junction initiated a cell rearrangement, the newly formed junction remained short and very often (85%) shrank shortly thereafter, giving rise to a short unstable junction as it kept on rearranging back and forth several times (Figures 3D, 3E, and S3M; Movie S2B). This demonstrates that PTEN loss of function prevents junction elongation during cell rearrangement and leads to unstable junctions, as predicted by our model and laser ablations.

To further establish whether the *pten* defects in junction remodeling is associated with the formation of short junctions, we categorized in both WT and *pten* tissues the distribution of the final junction length as a function of the number of cell rearrangements they underwent. In the WT tissue, independently of the number of cell rearrangements that a junction underwent, most of the junctions found at 29 hAPF are long junctions, lengths of which are close to the average length (Figure 3C). In *pten* tissue, nonrearranging junctions mainly produce long junctions, which length distribution is similar to the WT ones (dotted light red line in Figure 3F). In contrast, we observed that junctions having rearranged more than four times are the main source of the excess of short junctions observed in the *pten* tissue (dark red line in Figure 3F, 91% of the short junctions).

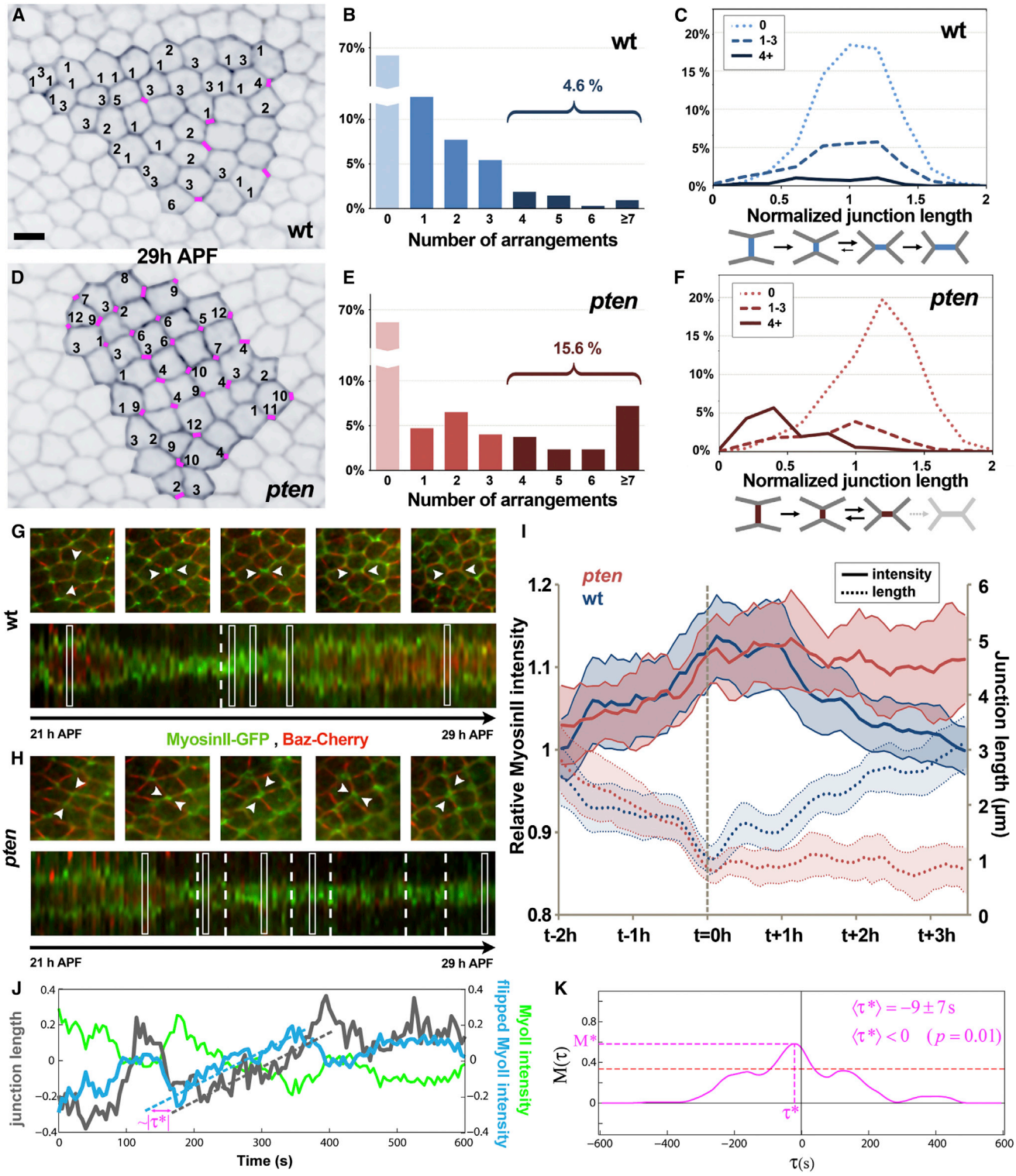

Figure 3. *pten* Cells Undergo Numerous Successive Cell Rearrangements, Giving Rise to Short Junctions Enriched in MyoII that Prevents Their Elongation

(A) Last confocal image of a 6 hr long (23–29 hAPF) E-Cad-GFP time-lapse movie in a WT tissue. 129 WT cell junctions were tracked. Junctions formed by cell rearrangement during the filmed period are labeled with the number of rearrangements they underwent. Short junctions (<0.5 × average length, n=6) are shown in magenta.

(B) Bar plot of cell junctions according to the number of cell rearrangements they underwent in WT tissue. 957 junctions were tracked. Light blue, nonrearranging junctions; blue, junctions undergoing one to three rearrangements; dark blue, junctions undergoing four or more cells rearrangements.

(legend continued on next page)

Taken together, our results demonstrate that the excess of short junctions observed in *pten* tissue is associated with a failure of junction lengthening during cell rearrangement accompanied by junction instability.

MyoII Is Enriched at Newly Formed Junctions during Cell Rearrangements

Our analyses have shown that the loss of PTEN activity is associated with: (1) an increased level of MyoII at short junctions, and (2) a failure of junction lengthening during cell rearrangement leading to the formation of unstable junctions. Because MyoII activity has been so far only linked to junction shortening during cell rearrangements that have been described as irreversible processes (Bertet et al., 2004; Rauzi et al., 2010; de Matos Simões et al., 2010; Zallen and Wieschaus, 2004), current models do not account for these two observations. We therefore explored MyoII dynamics during both junction shortening and lengthening using a functional GFP-tagged MyoII light chain (Royou et al., 2004) (Figures 3G and 3H). In WT wing tissue, MyoII-GFP intensity increased at the cell junction concomitantly to its shortening (Figure 3G). When the rearranging cells formed a 4-fold vertex, MyoII-GFP became strongly concentrated all around this vertex, suggesting that the four cells contributed to this enrichment (Figure 3G). Consistent with this, we detected a strong MyoII-GFP signal at the newly formed junction that faded as the junction lengthened (Figure 3G; Movie S2C). Accordingly, the quantification of MyoII-GFP signal during junction elongation revealed a striking correlation between the decrease of MyoII-GFP concentration and the elongation of the newly formed junction (blue in Figure 3I, n = 24). Fast time-lapse imaging of MyoII-GFP dynamics during junction elongation confirmed an inverse correlation between MyoII-GFP level and junction length at short timescale (Figure 3J). Moreover, the analysis of time correlations between MyoII-GFP dynamics and junction length dynamics establishes that the reduction of MyoII-GFP levels at the junction precedes junction elongation by 9 ± 7 s (n = 7, $p < 0.01$; Figures 3K and S3N–S3O′), ruling out that the decrease in MyoII-GFP level is a consequence of junction elongation.

In *pten* tissue, no defects in MyoII-GFP accumulation or junction length were observed during junction shrinkage (Figures 3H, red in 3I, n = 14; Movie S2D). However, following the 4-fold vertex stage, MyoII-GFP remained concentrated all along the short junctions, which failed to elongate and kept on rearranging (Figure 3H, red in 3I, n = 14; Movie S2D). The results demonstrate that in WT tissue, MyoII is unexpectedly enriched at newly formed junctions and that its concentration decreases during junction elongation in a PTEN-dependent manner.

PIP3 Levels Decrease during Junction Elongation

We then explored the dynamics of PIP3 during cell rearrangements. We observed that the specific PIP3 probe, the PH domain (for Pleckstrin homology) of GRP1 fused to GFP ($PH_{(PIP3)}$-GFP) (Britton et al., 2002), accumulates at the newly formed junction and its level decreases as the junction elongates (Figures 4A and 4C). As expected, in *pten* tissue, the overall PIP3 level was increased at the cell membrane relative to the WT tissue (Figure S4A). Moreover, we found that the relative level of PIP3 increased during junction shortening. However, in *pten* tissue PIP3 level failed to significantly decrease at the unstable rearranging junctions that do not regrow (Figures 4B and 4C). These results further argue for a regulatory role of PTEN during junction elongation.

Rok Activity Is Required for the Short Junction Phenotype in *pten* Tissue

MyoII activity is positively and negatively controlled by regulators that therefore modulate cortical tension (Clark et al., 2007). Rho-kinase (Rok) is an essential regulator of MyoII activity (Amano et al., 2010; Winter et al., 2001). We therefore generated a functional Rok-GFP transgene and imaged the dynamics of Rok-GFP during junction remodeling. In WT tissue, Rok-GFP is transiently enriched at newly formed junctions and decreases as junctions lengthen, as observed for MyoII-GFP (Figures 4D and 4F,

(C) Histogram of the distribution of junction lengths categorized according to the number of cell rearrangements they underwent in WT tissue. The color code used is the same as in (B). Below the histogram, a schematic of the typical rearrangement process in a WT tissue is shown.
(D) Last confocal image of 6 hr long (23–29 hAPF) E-Cad-GFP time-lapse movie in a $pten^{RNAi}$ tissue. 127 $pten^{RNAi}$ cell junctions were tracked. Junctions formed by cell rearrangement during the filmed period are labeled with the number of rearrangements they underwent. Short junctions (<0.5 × average length, n = 28) are shown in magenta.
(E) Bar plot of cell junctions according to the number of cell rearrangements they underwent in $pten^{RNAi}$ tissue. 723 junctions were tracked. Light red, non-rearranging junctions; red, junctions undergoing one to three rearrangements; dark red, junctions undergoing four or more cells rearrangements.
(F) Histogram of the distribution of junction lengths categorized according to the number of cell rearrangements they underwent in $pten^{RNAi}$ tissues. The color code used is the same as in (E). Below the histogram, a schematic of the typical rearrangement process in $pten^{RNAi}$ tissue is shown.
(G and H) Representative images (top panels) and kymographs (bottom panels) of MyoII-GFP (green) and Bazooka-Cherry (Baz-Cherry, red) time-lapse imaging during cell rearrangements in WT (G) and $pten^{RNAi}$ (H) tissues. Top panels: the tracked junctions are highlighted by arrowheads. Bottom panels: white rectangular boxes outline the successive temporal positions corresponding to the images shown in the above panels. White dashed bars: timings of 4-fold vertices created by cell rearrangements.
(I) Graph of the average relative intensity of MyoII-GFP (solid lines with SD shown as a shaded region) and of the junction length (dashed lines with the SD shown as shaded region) during cell rearrangements in a WT tissue (blue) and in a $pten^{RNAi}$ tissue (red).
(J) Graph of time evolution of relative junction length $L(t)$ (gray) and relative MyoII-GFP intensity $MyoII(t)$ (green) determined by high time-resolution time-lapse video (12 frames min^{-1}). Because MyoII-GFP intensity and junction length are anticorrelated, MyoII-GFP intensity was flipped to $-MyoII(t)$ (blue; see Supplemental Experimental Procedures) to emphasize and measure the time delay between MyoII-GFP and junction length dynamics.
(K) Delay function $M(\tau)$ (that compares $L(t)$ to $MyoII(t+\tau)$; see Supplemental Experimental Procedures; Figure S3) reaches a maximum M^* for the value of the time delay τ minimizing the area between the two curves ($\tau^* = -21$ s for the curves in J). Seven out of eight analyses displayed a correlation between variations of *MyoII* and *L* ($M^* > M_{random} = 0.33$, dashed red line), and yielded a significantly negative average value $<\tau^*> = -9 \pm 7$ s (n = 7, $p < 0.01$), showing that MyoII intensity variations precede junction length variations.
Scale bar represents 5 μm. See also Figure S3 and Movies S1 and S2.

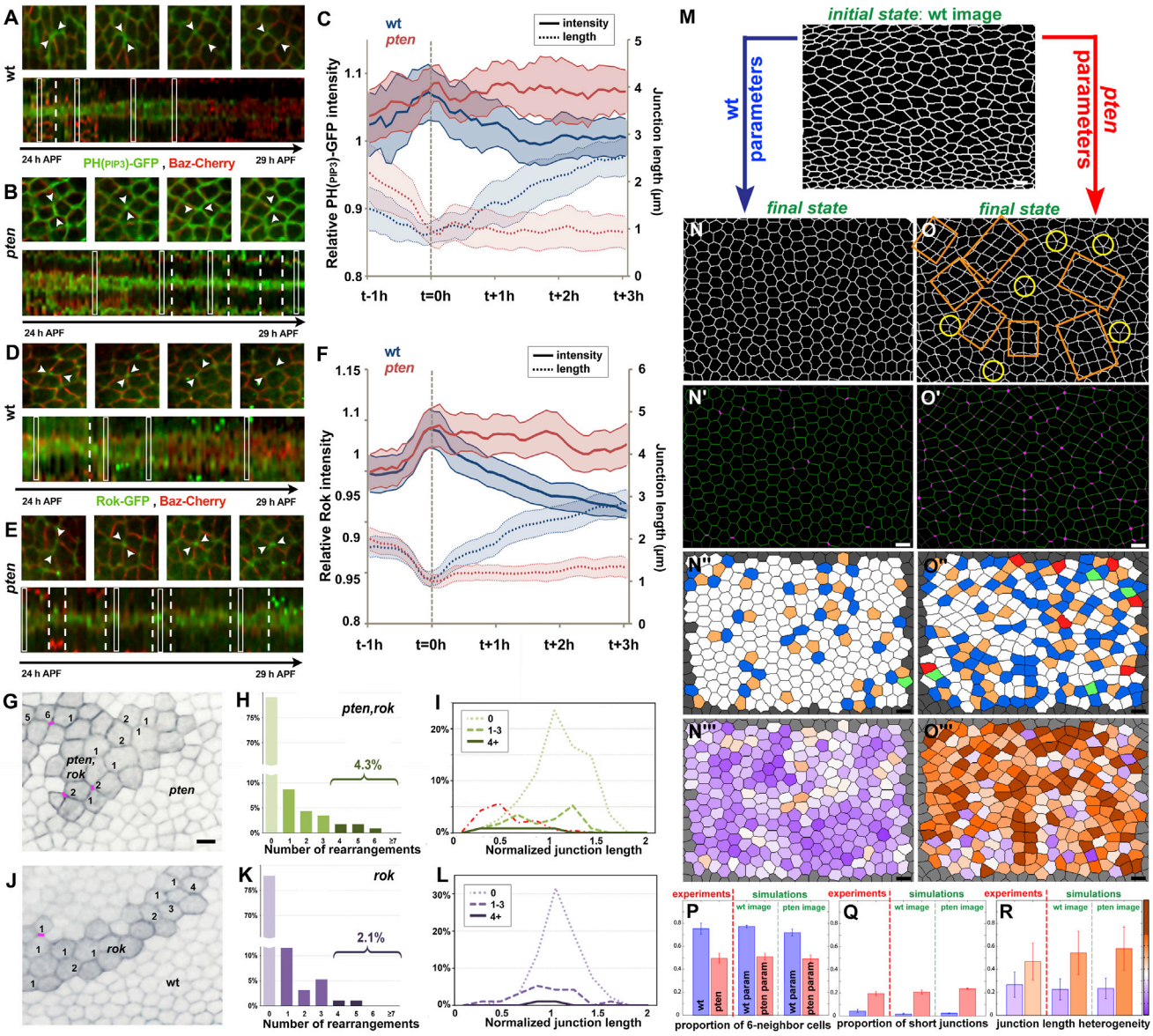

Figure 4. Maintenance of Cortical Tension Accounts for the *pten* Phenotypes

(A and B) Representative images (top panels) and kymographs (bottom panels) of PH(PIP3)-GFP (green) and Baz-Cherry (red) time-lapse imaging during cell rearrangements in WT (A) and $pten^{RNAi}$ (B) tissues. Top panels: the tracked junction is highlighted by arrowheads. Bottom panels: white rectangular boxes outline the successive temporal positions corresponding to the images shown in the above panels. White dashed bars: timings of 4-fold vertices created by cell rearrangements.

(C) Graphs of average relative intensity of PH(PIP3)-GFP (solid lines and SD shown as a shaded region) and of junction length (dashed lines and SD shown as shaded region) during cell rearrangement in a WT (blue) and $pten^{RNAi}$ (red) tissues.

(D and E) Typical images (top panels) and kymographs (bottom panels) of Rok-GFP (green) and Baz-Cherry (red) time-lapse imaging during cell rearrangements in WT (D) and $pten^{RNAi}$ (E) tissue. Top panels: the tracked junction is highlighted by arrowheads. Bottom panels: white rectangular boxes outline the successive temporal positions corresponding to the images shown in the above panels. White dashed bars: timings of 4-fold vertices created by cell rearrangements.

(F) Graph of average relative intensity of Rok-GFP (solid lines with SD shown as a shaded region) and of junction length (dashed lines) during cell rearrangement in WT (blue) and $pten^{RNAi}$ (red) tissues.

(G) Last confocal images of a 6 hr long (23–29 hAPF) E-Cad-GFP time-lapse movie of a representative rok^{2} clone in a $pten^{RNAi}$ tissue. A total of 115 rok^{2}, $pten^{RNAi}$ cell junctions were tracked. Junctions formed by cell rearrangement during the filmed period are labeled with the number of rearrangements they underwent. Short junctions (<0.5 × average length, n = 3) are shown in magenta.

(H) Bar plot of cell junctions according to the number of cell rearrangements they underwent in $pten^{RNAi}$, rok^{2} tissue. A total of 115 junctions were tracked. Light green, nonrearranging junctions; green, junctions undergoing one to three rearrangements; dark green, junctions undergoing four or more cells rearrangements.

(I) Histogram of the distribution of junction lengths in $pten^{RNAi}$, rok^{2} tissue categorized according to the number of rearrangements they underwent. The color code used is the same as in (H). For comparison, the dashed red line (I) represents the distribution of the short and highly rearranging junctions lengths in *pten* tissue.

(legend continued on next page)

n = 27). Conversely, in *pten* tissue, Rok-GFP intensity remained high at the newly formed junctions that failed to elongate (Figures 4E and 4F, n = 24).

Having found that MyoII-GFP level decreases prior to junction elongation, we investigated whether the downregulation of MyoII activity was necessary for junction elongation during cell rearrangement by testing whether a loss of Rok activity could suppress the PTEN loss of function phenotypes. To this end, we generated small *rok* clones in a $pten^{RNAi}$ tissue and analyzed both the cell packing and the cell rearrangement dynamics. In such experimental conditions, cytokinesis did not seem to be impaired because cell apical areas were only mildly increased, likely due to a loss of contractility associated with an observed decrease of MyoII cortical localization (Figure S4B). Noticeably, we found that *rok* clones generated in *pten* tissue suppressed the effect of PTEN loss of function on cell packing, namely the excess of short junctions (Figure 4G; purple line in Figure S4C). Despite a slightly higher proportion of nonrearranging junctions (1.15-fold), the rearranging junctions neither produced an excess of short junctions nor fluctuated extensively, but lengthened to produce long cell junctions as observed in the WT tissue (Figures 4H–4I). Furthermore, the packing and cell rearrangement dynamics in double *pten*, *rok* tissue is similar to the one observed in *rok* single mutant tissue (Figures 4J–4L; green line in Figure S4C). This genetic evidence demonstrates that Rok is needed to induce the cell rearrangement and packing defects observed in *pten* tissue. Together with our analysis of MyoII and Rok dynamics during cell rearrangement, our results strongly indicate that PTEN is necessary to downregulate MyoII activity during cell rearrangement.

Altogether our results uncover PTEN as a specific regulator of junction lengthening and stability during cell rearrangement. Furthermore they support a mechanism whereby PTEN regulates the PIP3 levels at newly formed junction to decrease Rok-dependent MyoII contractility, thereby promoting junction lengthening and stabilization.

Maintenance of High Tension in Newly Formed Junctions Accounts for *pten* Cobblestone and Rosette Packing

Having found that PTEN locally regulates cell junction contractility during cell rearrangements, we investigated whether this local role was sufficient to explain the cobblestone and rosette patterns observed at the global level in *pten* tissue. To this end, we performed computer simulations based on the cellular Potts model that is a general algorithm to simulate groups of cells and to capture the disordered nature of epitheliums (Graner and Glazier, 1992; Krieg et al., 2008). To take into account the proximal-distal elongation of wing cells due to hinge contraction (Aigouy et al., 2010), we started the simulations with a segmented image of an actual WT tissue at 24 hAPF, and we let this tissue evolve to a minimum of energy with the two distinct sets of λ side parameters previously inferred from our laser ablations in WT and *pten* tissues (Figures 2E, S2D, and S2E). In the WT case, each junction was assigned the same λ parameter (λ_o = 2.3). Alternatively, in the *pten* case, we used two distinct λ parameters (λ_L = 2.9 and λ_S = 1.8). Indeed, because our experimental results showed that shorter junctions, including newly formed ones, are under higher tension due to higher level of MyoII (Figures 2D, 2G, 2H, and 3I), we assigned λ_S to the shortest sides ($l \leq 0.5$) and newly formed ones, and λ_L to the longest sides in initial image ($l > 0.5$). Numerical simulations starting from WT segmented images at 24 hAPF and run with WT parameters displayed a relaxation of elongated cell shapes via cell rearrangements and yielded final patterns in very good agreement with the experimental WT honeycomb-like packing at 30 hAPF (Figures 4M and 4N–4N‴; Movie S3A–A‴). In sharp contrast, simulations starting from the same WT images but run with the *pten* parameters displayed many sides that failed to lengthen and to complete cell rearrangements, and yielded final patterns displaying typical cobblestone and rosette patterns, like the ones observed in *pten* tissue (Figures 4M, 4O–4O‴; Movie S3B–S3B‴). The quantitative analysis of these simulated final packings displayed final proportions of six neighbor cells, short junctions, and junction length heterogeneity very similar to those observed in WT and *pten* tissues at 30 hAPF (Figures 4P–4R). Interestingly, the same results were obtained in simulations starting with a segmented image of *pten* tissue at 24 hAPF (Figures 4P–4R and S4D–S4F‴). Taken together, our results show that the local maintenance of high tension in newly formed junctions can account for the global cobblestone and rosette packing characterizing *pten* wings.

(J) Last confocal image of a 6 hr long (23–29 hAPF) E-Cad-GFP time-lapse movie of a representative rok^2 clones in a WT tissue. A total of 95 rok^2 cell junctions were tracked. Junctions formed by cell rearrangement during the filmed period are labeled with the number of rearrangements they underwent. Short junctions (<0.5 × average length, n = 1) are shown in magenta.

(K) Bar plot of cell junctions according to the number of cell rearrangements they underwent in a representative rok^2 clone in a WT tissue. A total of 95 junctions were tracked. Light purple, nonrearranging junctions; purple, junctions undergoing one to three rearrangements; dark purple, junctions undergoing four or more rearrangements.

(L) Histogram of the distribution of junction lengths in rok^2 tissue categorized according to the number of rearrangements they underwent. The color code used is the same as in (K).

(M–O‴) Numerical simulations of WT and *pten* tissues. Segmented experimental image of WT tissue at 24 hAPF used as initial state by both simulations using parameters of WT (blue arrow) and pten (red arrow) (M). Typical final state of simulations run with WT parameters resulting in honeycomb-like packing (N) and displaying few short junctions (N′), a small disorder in number of neighbors (N″), and a low junction length heterogeneity (N‴). Color codes as in Figure 1. Typical final state of simulations run with pten parameters resulting in cobblestone (orange) and rosette (yellow) packing (O), and many short junctions (O′), a large disorder of number of neighbors (O″), and a large junction length heterogeneity (O‴). Color codes as in Figure 1.

(P–R) Comparison of quantitative analyses of cell packings in experimental WT and *pten* tissues at 28–30 hAPF (left in P–R; data from Figures 1D, 1F, and 1H), in simulations run with WT and *pten* parameters starting with segmented images from WT tissue (n = 3 simulations) (middle in P–R), and in simulations run with WT and *pten* parameters starting with segmented images from *pten* tissue (right in P–R) (n = 4 simulations). Bars indicate the SD of distributions. (P) Proportion of six neighbor cells. (Q) Proportion of normalized junction lengths satisfying $l < 0.5$. (R) Cellular junction length heterogeneity.

Scale bars represent 5 μm. See also Figure S4 and Movie S3.

Defects in Junction Elongation and Hexagonal Packing Are Associated with Defects in Tissue Morphogenesis, Tissue Planar Polarization, and Tissue Architecture

The identification of *pten* as a regulator of both junction dynamics during cell rearrangements and of cell regular hexagonal shapes in the wing gives the opportunity to study the contribution of these processes to tissue morphogenesis, PCP, and organ architecture (ridges of the wing cuticle in this study). We first analyzed the contribution of PTEN to tissue dynamics and morphogenesis between 24 and 29 hAPF, a period over which we have characterized the role of PTEN in junction dynamics, and during which the tissue packing becomes honeycomb-like (Aigouy et al., 2010; Classen et al., 2005). We compared tissue deformation and the underlying cell dynamics in terms of cell rearrangements and cell shape changes in WT and *pten* tissues by applying a quantitative framework that we have developed and validated recently (Figures 5A–5A″; Supplemental Experimental Procedures) (Bosveld et al., 2012). We found that the WT tissue displays important contributions of both AP oriented cell rearrangements and PD oriented cell contraction (Figures 5B and 5C; see also Aigouy et al., 2010). Strikingly, these contributions cancel out, showing that AP cell rearrangements compensate the PD cell contraction, leading to the formation of regular hexagons without significant change in tissue shape ("wt" in Figure 5C and sketch in Figure 5A″). Performing the same analysis on *pten* tissue and subtracting it from the WT analysis enabled us to isolate the defects associated with PTEN loss of function (Bosveld et al., 2012). In agreement with our results on the role of PTEN in junction dynamics and cell packing, PTEN loss of function results in significant defects in both cell rearrangements and cell shape changes. Importantly, these two processes do not cancel out anymore, leading to a defect in tissue contraction along a direction pointing upward the PD axis ("wt-*pten*" in Figure 5C). Accordingly, PTEN loss of function results in adult wings that are slightly more elongated along this direction than the WT ones (Figure 5D). Our analysis of tissue morphogenesis in WT and *pten* wings therefore illustrates that cell rearrangements play a role in coordinating the dynamics of individual cells and the shape of the global tissue.

To test the role of cell rearrangements for the fine-tuning of global PCP alignment along the wing P-D axis (Aigouy et al., 2010), we then determined the intensity, the individual cell planar polarization and the global tissue polarization using Stbm-YFP as a PCP marker (Bellaïche et al., 2004). Although the intensity and the individual cell polarization were similar in WT and *pten* cells, the global tissue PCP relative to the PD axis was significantly affected in absence of *pten* function (Figures 5E–5H). Finally, the regular hexagonal cell packing is proposed to have a key contribution to generate ridges of the adult wing cuticle that are proposed to impact the tissue architecture and mechanics (Doyle et al., 2008). We found that loss of PTEN function drastically affect the ridge organization in the adult wing (Figures 5I and 5J). Collectively, the characterization of the function of PTEN in cell rearrangements establishes the contribution of cell rearrangements to the establishment of the final tissue and cell shapes, PCP global polarization and tissue architecture.

CONCLUSION

Previous studies of junction remodeling established that the dynamics of acto-myosin network generates the cortical contractile forces necessary for junction shortening (Bertet et al., 2004; Rauzi et al., 2008; de Matos Simões et al., 2010; Zallen and Wieschaus, 2004) and implicitly assumed that junction elongation is a passive relaxation process that does not involve any specific regulation (Aigouy et al., 2010; Farhadifar et al., 2007; Glazier and Graner, 1993; Hilgenfeldt et al., 2008; Käfer et al., 2007; Rauzi et al., 2008). Here, we identified PTEN as a specific regulator of junction elongation and stability during cell rearrangement. We observed that the newly formed junction is initially enriched in MyoII and PIP3, which is consistent with the MyoII and PI3K recruitments observed upon E-cad engagement in cell culture models (Papusheva and Heisenberg, 2010). However, in such models, Rok-dependent MyoII contractility is usually proposed to promote junction expansion by pulling on junction edges (Yamada and Nelson, 2007). In an epithelial tissue, our work uncovered that junction lengthening is coupled to the PTEN-dependent decrease of cortical distribution of MyoII that leads to the restoration of an homogeneous cortical contractility around the cortex of cells. This homogenous distribution is required for the formation of a stable, honeycomb-like cell packing as observed in several epithelial tissues (Classen et al., 2005; Farhadifar et al., 2007; Gibson et al., 2006; Narimatsu et al., 2009; Tardieu, 1988). Our findings thus establish that junction elongation is a PTEN-controlled process acting as a critical regulatory step during cell rearrangement. Two nonmutually exclusive models can account for the temporal and spatial regulation of PIP3 level during junction elongation by PTEN. (1) As observed in cell culture upon cell-cell contact formation (Perez et al., 2008; reviewed in Rivard, 2009), PI3K-dependent increase of PIP3 level at the cell-cell contact can be antagonized by a homogenous activity of PTEN at the cell junction, and (2) the activity of PTEN or its recruitment might be regulated locally during junction elongation. Interestingly, the Rok kinase was shown to phosphorylate PTEN and to trigger its activation during cell migration (Li et al., 2005), suggesting a model whereby the initial activation of Rok can initiate a negative feedback loop to promote local activation to PTEN, hence junction elongation and reduction of cortical tension.

Our work also highlights that cellular pattern formation involves reversibility and fluctuations of rearrangements, which could provide the tissue with a mean to explore the energy landscape of cellular patterns. We foresee that mechanisms promoting MyoII homogenous distribution could be more general and drive the restoration of cell contractility symmetry following cell polarization and cell cytokinesis.

EXPERIMENTAL PROCEDURES

Fly Stocks, Genetics, and Molecular Biology

The stocks used were obtained from the Bloomington Stock Center and raised at 25°C, unless otherwise mentioned. All stocks and associated references are described in the Supplemental Experimental Procedures. Loss of function clones were generated using the hs-FLP/FRT system (Xu and Rubin, 1993). Typically, heat shocks of 15 min (for *pten* mutant clones) or 1 hr were carried out 3 days before pupa formation (BPF). White pupae were picked and timed

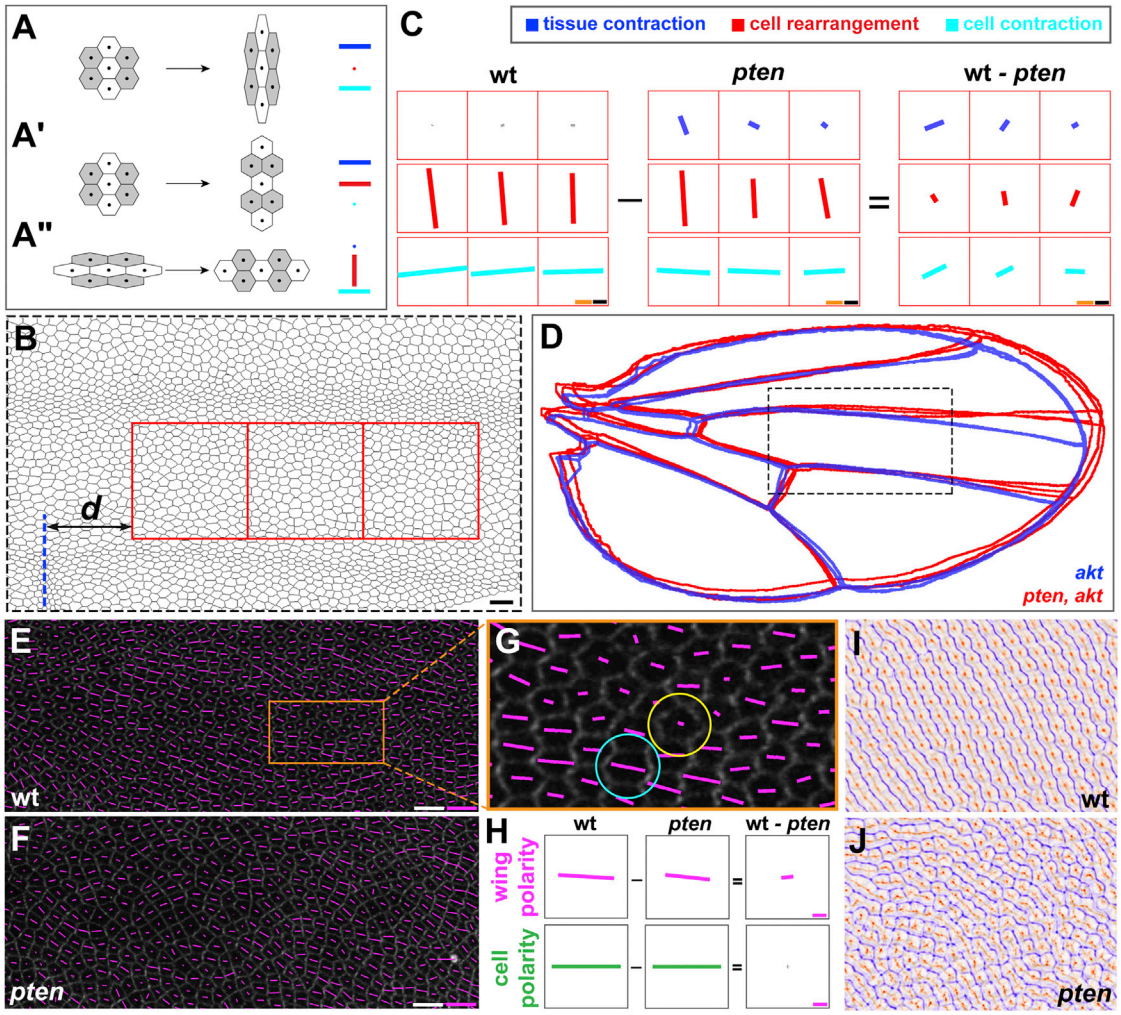

Figure 5. Role of PTEN in Tissue Morphogenesis, PCP, and Tissue Architecture

(A–A″) Framework for quantitative analysis of tissue contraction-extension (blue), cell-cell rearrangements (red), and cell shape changes (cyan; see Experimental Procedures). (A and A′) The patch of tissue undergoes the same contraction-extension through pure cell shape changes (A), and through pure cell rearrangements (A′). (A″) Initial cell elongation vanishes through cell rearrangements occurring in the perpendicular direction and resulting in regular hexagons and no tissue deformation.

(B) Segmented image of wing (29 hAPF). Red square boxes (54 × 54 μm^2) indicate the regions where quantitative analysis was performed. d = 40 μm.

(C) Comparative analysis of morphogenesis in WT and *pten* wings. Subtractive analysis ("wt-*pten*") shows that PTEN loss of function results in weaker cell rearrangements and cell shape changes: (1) oscillating junctions reduce the net contribution of cell rearrangements, and (2) the disruption of junction elongation prevents the complete relaxation of cell elongated shapes into regular hexagons, thus resulting in a weaker oriented contraction of cells in a direction slightly tilted with respect to the PD axis. Overall, this corresponds to a defect of tissue contraction along this direction, which is consistent with wing shape defects observed in (D). Significant data are plotted with thick color bars, nonsignificant data with gray bars (see Experimental Procedures) (Bosveld et al., 2012), averages done over n = 2 WT and n = 2 *pten* wings.

(D) Outlines of three adult wings from akt^1/akt^3 flies (blue) and $akt^1/akt,^3pten^{117}$ flies (red) were overlaid. akt^1/akt^3 tissue do not show packing defects as opposed to $akt^1/akt,^3pten^{117}$ tissue (Figures S1D and S1F). The comparison of akt^1/akt^3 and $akt^1/akt,^3pten^{117}$ wings permits to determine the function of *pten* on tissue morphogenesis independently of its role in tissue growth. Dashed box indicates region in (B).

(E and F) Quantification on images of fixed wings at 30 hAPF of local and global PCP of Stbm protein (Stbm-YFP, in gray) in WT (E) and *pten* (F) wings. Each bar (magenta) represents the amplitude and direction of the anisotropy in Stbm junctional localization around each cell.

(G) Close up of a region in (E) showing examples of cells displaying a weak polarity of Stbm intensity resulting in a small bar (yellow circle), and a strong anisotropy yielding a large bar in the direction of polarization (cyan circle). The intensity level (IL) of each pixel in Stbm (0 < IL < 255) around the cell cortex was used to characterize cell polarity (see Experimental Procedures).

(H) Averages of Stbm polarity in WT and *pten* wings. The "wing polarity" characterizes the coordination of cell polarities across the wing. The "cell polarity" quantifies the polarization of Stbm distribution in each cell. Subtractive analysis shows a significant difference in wing polarity between WT and *pten* tissues, but no difference in Stbm cell polarity (average over n = 3 WT wings, n = 3 *pten* wings, with $\langle n_{cells} \rangle \approx 1{,}040$ analyzed cells per wing).

(I and J) Using cuticles refraction microscopy (Doyle et al., 2008), the ridges on adult wing cuticle that characterize the architecture of wing tissue were determined in WT and *pten* tissues. Images are superposition of the dorsal (purple) and the ventral (orange) ridges in WT wings (I) and $pten^{RNAi}$ wings (J).

Scale bars represent 10 μm (B and C, black bars; E and F, white bars); 2 μm^2 min^{-1} (C, orange bars); IL = 50 (E and F), IL = 2 (H), magenta bars.

at 25°C before dissection. For *rok* clones, heat shocks were performed 2 days BPF to obtain small clones mostly devoid of very large cells. Ubi-GFP-Rok was generated by cloning under the control of Ubiquitin 63E promoter a full-length *rok* cDNA downstream of GFP in a P element vector. Ubi-GFP-Rok rescues the rok^2 null allele in somatic clones.

Immunostaining

Wing dissection, fixation, and immunostaining were carried out as described (Classen et al., 2008). Antibodies are rat anti-E-cad (1:50; Developmental Studies Hybridoma Bank), mouse anti-FasciclinIII (1:50; DSHB), rat anti-Crumbs (1:1000, gift of U. Tepass), mouse anti-Discs-large (1:1000; DSHB), Alexa Fluor 488-, 555-conjugated secondary antibodies (Molecular Probes), and Cy5-conjugated secondary antibodies (Jackson ImmunoResearch). Images were acquired on a laser-scanning confocal microscope (LSM710, Zeiss).

Time-Lapse Experiments

Timed pupae were dissected, mounted and imaged as previously described for the fly thorax (Gho et al., 1999), acquiring one z stack of images for each channel every 5 min. The en-GAL4 driver was used to express the *pten* dsRNA in the posterior wing. For the time-lapse experiments with E-cad-GFP, $Gal80^{ts}$ was used for temporal control of the dsRNA expression. Larvae were raised at 18°C, and shifted at 29°C 1 day BPF, affecting the PTEN function during pupal development. Developmental times were corrected to match the 25°C reference, using a coefficient of 0.79. Images were acquired with a Ropper spinning-disk confocal mounted on an Eclipse Ti microscope (Nikon) using the Metamorph software.

Laser Ablations

Both wild-type and *pten* mutant clone cells were labeled with E-cad-GFP. A 2-photon Mai-Tai laser (890 nm, 100 mW, 2 repetitions) ablated a cell junction (Hutson and Ma, 2007) on NLO LSM710 (Zeiss). Junction ablations and initial velocity quantifications were carried out as in Bosveld et al. (2012).

Image Treatments, Quantification, Intensity Measurement, and Cell Junction Tracking

For detailed information on image treatments, quantification, intensity measurement, and cell junction tracking, see the Supplemental Experimental Procedures.

SUPPLEMENTAL INFORMATION

Supplemental Information includes Supplemental Experimental Procedures, four figures, and three movies and can be found with this article online at http://dx.doi.org/10.1016/j.devcel.2013.04.020.

ACKNOWLEDGMENTS

We thank E. Hafen, H. Hong, R. Karess, E. Martin-Blanco, H. Oda, F. Pichaud, U. Tepass, C. Wilson, E. Wieschaus, J. Zallen, the Developmental Studies Hybridoma Bank, the Bloomington Stock Center, and TRiP at Harvard Medical School (NIH/NIGMS R01-GM084947) for strains and antibodies; the Curie Imaging Facility (PICT-IBiSA@BDD); J. Käfer for advice with computer simulations; and V. Hakim, E. Heard, J. Käfer, A-M. Lennon, and J.-P. Vincent for critical comments on the manuscript. This work is supported by the FRM (26329) and the INCA (4731); by grants to Y.B. from the ARC (4830), the ANR (BLAN07-3-207540, MorphoDro), and an ERC Starting Grant (CePoDro 209718); and by the CNRS, INSERM, and the Curie Institute. P-L.B. is supported by an INSERM postdoctoral fellowship.

Received: August 4, 2012
Revised: March 12, 2013
Accepted: April 22, 2013
Published: May 23, 2013

REFERENCES

Aigouy, B., Farhadifar, R., Staple, D.B., Sagner, A., Röper, J.C., Jülicher, F., and Eaton, S. (2010). Cell flow reorients the axis of planar polarity in the wing epithelium of Drosophila. Cell *142*, 773–786.

Amano, M., Nakayama, M., and Kaibuchi, K. (2010). Rho-kinase/ROCK: a key regulator of the cytoskeleton and cell polarity. Cytoskeleton *67*, 545–554.

Bellaïche, Y., Beaudoin-Massiani, O., Stuttem, I., and Schweisguth, F. (2004). The planar cell polarity protein Strabismus promotes Pins anterior localization during asymmetric division of sensory organ precursor cells in Drosophila. Development *131*, 469–478.

Bertet, C., Sulak, L., and Lecuit, T. (2004). Myosin-dependent junction remodelling controls planar cell intercalation and axis elongation. Nature *429*, 667–671.

Bosveld, F., Bonnet, I., Guirao, B., Tlili, S., Wang, Z., Petitalot, A., Marchand, R., Bardet, P.-L., Marcq, P., Graner, F., and Bellaïche, Y. (2012). Mechanical control of morphogenesis by Fat/Dachsous/Four-jointed planar cell polarity pathway. Science *336*, 724–727.

Britton, J.S., Lockwood, W.K., Li, L., Cohen, S.M., and Edgar, B.A. (2002). Drosophila's insulin/PI3-kinase pathway coordinates cellular metabolism with nutritional conditions. Dev. Cell *2*, 239–249.

Chalhoub, N., and Baker, S.J. (2009). PTEN and the PI3-kinase pathway in cancer. Annu. Rev. Pathol. *4*, 127–150.

Clark, K., Langeslag, M., Figdor, C.G., and van Leeuwen, F.N. (2007). Myosin II and mechanotransduction: a balancing act. Trends Cell Biol. *17*, 178–186.

Classen, A.K., Anderson, K.I., Marois, E., and Eaton, S. (2005). Hexagonal packing of Drosophila wing epithelial cells by the planar cell polarity pathway. Dev. Cell *9*, 805–817.

Classen, A.K., Aigouy, B., Giangrande, A., and Eaton, S. (2008). Imaging Drosophila pupal wing morphogenesis. Methods Mol. Biol. *420*, 265–275.

de Matos Simões, S., Blankenship, J.T., Weitz, O., Farrell, D.L., Tamada, M., Fernandez-Gonzalez, R., and Zallen, J.A. (2010). Rho-kinase directs Bazooka/Par-3 planar polarity during Drosophila axis elongation. Dev. Cell *19*, 377–388.

Doyle, K., Hogan, J., Lester, M., and Collier, S. (2008). The Frizzled planar cell polarity signaling pathway controls Drosophila wing topography. Dev. Biol. *317*, 354–367.

Farhadifar, R., Röper, J.C., Aigouy, B., Eaton, S., and Jülicher, F. (2007). The influence of cell mechanics, cell-cell interactions, and proliferation on epithelial packing. Curr. Biol. *17*, 2095–2104.

Fernandez-Gonzalez, R., de Matos Simões, S., Röper, J.C., Eaton, S., and Zallen, J.A. (2009). Myosin II dynamics are regulated by tension in intercalating cells. Dev. Cell *17*, 736–743.

Gho, M., Bellaïche, Y., and Schweisguth, F. (1999). Revisiting the Drosophila microchaete lineage: a novel intrinsically asymmetric cell division generates a glial cell. Development *126*, 3573–3584.

Gibson, M.C., Patel, A.B., Nagpal, R., and Perrimon, N. (2006). The emergence of geometric order in proliferating metazoan epithelia. Nature *442*, 1038–1041.

Glazier, J.A., and Graner, F. (1993). Simulation of the differential adhesion driven rearrangement of biological cells. Phys. Rev. E *47*, 2128–2154.

Graner, F., and Glazier, J.A. (1992). Simulation of biological cell sorting using a two-dimensional extended Potts model. Phys. Rev. Lett. *69*, 2013–2016.

Graner, F., and Sawada, Y. (1993). Can surface adhesion drive cell rearrangement? Part II: a geometrical model. J. Theor. Biol. *164*, 477–506.

Hales, T.C. (2001). The honeycomb conjecture. Disc. Comp. Geom. *25*, 1–22.

Harumoto, T., Ito, M., Shimada, Y., Kobayashi, T.J., Ueda, H.R., Lu, B., and Uemura, T. (2010). Atypical cadherins Dachsous and Fat control dynamics of noncentrosomal microtubules in planar cell polarity. Dev. Cell *19*, 389–401.

Hilgenfeldt, S., Erisken, S., and Carthew, R.W. (2008). Physical modeling of cell geometric order in an epithelial tissue. Proc. Natl. Acad. Sci. USA *105*, 907–911.

Hutson, M.S., and Ma, X. (2007). Plasma and cavitation dynamics during pulsed laser microsurgery in vivo. Phys. Rev. Lett. *99*, 158104.

Hutson, M.S., Veldhuis, J., Ma, X., Lynch, H.E., Cranston, P.G., and Brodland, G.W. (2009). Combining laser microsurgery and finite element modeling to assess cell-level epithelial mechanics. Biophys. J. *97*, 3075–3085.

Käfer, J., Hayashi, T., Marée, A.F., Carthew, R.W., and Graner, F. (2007). Cell adhesion and cortex contractility determine cell patterning in the Drosophila retina. Proc. Natl. Acad. Sci. USA *104*, 18549–18554.

Keller, R. (2006). Mechanisms of elongation in embryogenesis. Development *133*, 2291–2302.

Knox, A.L., and Brown, N.H. (2002). Rap1 GTPase regulation of adherens junction positioning and cell adhesion. Science *295*, 1285–1288.

Krieg, M., Arboleda-Estudillo, Y., Puech, P.H., Käfer, J., Graner, F., Müller, D.J., and Heisenberg, C.P. (2008). Tensile forces govern germ-layer organization in zebrafish. Nat. Cell Biol. *10*, 429–436.

Lecuit, T., and Lenne, P.F. (2007). Cell surface mechanics and the control of cell shape, tissue patterns and morphogenesis. Nat. Rev. Mol. Cell Biol. *8*, 633–644.

Lecuit, T., Lenne, P.F., and Munro, E. (2011). Force generation, transmission, and integration during cell and tissue morphogenesis. Annu. Rev. Cell Dev. Biol. *27*, 157–184.

Li, Z., Dong, X., Wang, Z., Liu, W., Deng, N., Ding, Y., Tang, L., Hla, T., Zeng, R., Li, L., and Wu, D. (2005). Regulation of PTEN by Rho small GTPases. Nat. Cell Biol. *7*, 399–404.

Ma, D., Amonlirdviman, K., Raffard, R.L., Abate, A., Tomlin, C.J., and Axelrod, J.D. (2008). Cell packing influences planar cell polarity signaling. Proc. Natl. Acad. Sci. USA *105*, 18800–18805.

Maître, J.L., Berthoumieux, H., Krens, S.F., Salbreux, G., Jülicher, F., Paluch, E., and Heisenberg, C.P. (2012). Adhesion functions in cell sorting by mechanically coupling the cortices of adhering cells. Science *338*, 253–256.

Martin-Belmonte, F., Gassama, A., Datta, A., Yu, W., Rescher, U., Gerke, V., and Mostov, K. (2007). PTEN-mediated apical segregation of phosphoinositides controls epithelial morphogenesis through Cdc42. Cell *128*, 383–397.

McGuire, S.E., Le, P.T., Osborn, A.J., Matsumoto, K., and Davis, R.L. (2003). Spatiotemporal rescue of memory dysfunction in Drosophila. Science *302*, 1765–1768.

McKenzie, E., Krupin, A., and Kelley, M.W. (2004). Cellular growth and rearrangement during the development of the mammalian organ of Corti. Dev. Dyn. *229*, 802–812.

Narimatsu, M., Bose, R., Pye, M., Zhang, L., Miller, B., Ching, P., Sakuma, R., Luga, V., Roncari, L., Attisano, L., and Wrana, J.L. (2009). Regulation of planar cell polarity by Smurf ubiquitin ligases. Cell *137*, 295–307.

Nishimura, T., Honda, H., and Takeichi, M. (2012). Planar cell polarity links axes of spatial dynamics in neural-tube closure. Cell *149*, 1084–1097.

Nowak, R.B., Fischer, R.S., Zoltoski, R.K., Kuszak, J.R., and Fowler, V.M. (2009). Tropomodulin1 is required for membrane skeleton organization and hexagonal geometry of fiber cells in the mouse lens. J. Cell Biol. *186*, 915–928.

Oda, H., and Tsukita, S. (2001). Real-time imaging of cell-cell adherens junctions reveals that Drosophila mesoderm invagination begins with two phases of apical constriction of cells. J. Cell Sci. *114*, 493–501.

Papusheva, E., and Heisenberg, C.P. (2010). Spatial organization of adhesion: force-dependent regulation and function in tissue morphogenesis. EMBO J. *29*, 2753–2768.

Perez, T.D., Tamada, M., Sheetz, M.P., and Nelson, W.J. (2008). Immediate-early signaling induced by E-cadherin engagement and adhesion. J. Biol. Chem. *283*, 5014–5022.

Pickering, K., Alves-Silva, J., Goberdhan, D., and Millard, T.H. (2013). Par3/Bazooka and phosphoinositides regulate actin protrusion formation during Drosophila dorsal closure and wound healing. Development *140*, 800–809.

Pinal, N., Goberdhan, D.C., Collinson, L., Fujita, Y., Cox, I.M., Wilson, C., and Pichaud, F. (2006). Regulated and polarized PtdIns(3,4,5)P3 accumulation is essential for apical membrane morphogenesis in photoreceptor epithelial cells. Curr. Biol. *16*, 140–149.

Rauzi, M., Verant, P., Lecuit, T., and Lenne, P.F. (2008). Nature and anisotropy of cortical forces orienting Drosophila tissue morphogenesis. Nat. Cell Biol. *10*, 1401–1410.

Rauzi, M., Lenne, P.F., and Lecuit, T. (2010). Planar polarized actomyosin contractile flows control epithelial junction remodelling. Nature *468*, 1110–1114.

Rivard, N. (2009). Phosphatidylinositol 3-kinase: a key regulator in adherens junction formation and function. Front. Biosci. *14*, 510–522.

Royou, A., Field, C., Sisson, J.C., Sullivan, W., and Karess, R. (2004). Reassessing the role and dynamics of nonmuscle myosin II during furrow formation in early Drosophila embryos. Mol. Biol. Cell *15*, 838–850.

Staple, D.B., Farhadifar, R., Röper, J.-C., Aigouy, B., Eaton, S., and Jülicher, F. (2010). Mechanics and remodelling of cell packings in epithelia. Eur. Phys. J. E. Soft Matter. *33*, 117–127.

Stocker, H., Andjelkovic, M., Oldham, S., Laffargue, M., Wymann, M.P., Hemmings, B.A., and Hafen, E. (2002). Living with lethal PIP3 levels: viability of flies lacking PTEN restored by a PH domain mutation in Akt/PKB. Science *295*, 2088–2091.

Tardieu, A. (1988). Eye lens proteins and transparency: from light transmission theory to solution X-ray structural analysis. Annu. Rev. Biophys. Biophys. Chem. *17*, 47–70.

Togashi, H., Kominami, K., Waseda, M., Komura, H., Miyoshi, J., Takeichi, M., and Takai, Y. (2011). Nectins establish a checkerboard-like cellular pattern in the auditory epithelium. Science *333*, 1144–1147.

Warrington, S.J., Strutt, H., and Strutt, D. (2013). The Frizzled-dependent planar polarity pathway locally promotes E-cadherin turnover via recruitment of RhoGEF2. Development *140*, 1045–1054.

Winter, C.G., Wang, B., Ballew, A., Royou, A., Karess, R., Axelrod, J.D., and Luo, L. (2001). Drosophila Rho-associated kinase (Drok) links Frizzled-mediated planar cell polarity signaling to the actin cytoskeleton. Cell *105*, 81–91.

Xu, T., and Rubin, G.M. (1993). Analysis of genetic mosaics in developing and adult Drosophila tissues. Development *117*, 1223–1237.

Yamada, S., and Nelson, W.J. (2007). Localized zones of Rho and Rac activities drive initiation and expansion of epithelial cell-cell adhesion. J. Cell Biol. *178*, 517–527.

Zallen, J.A., and Wieschaus, E. (2004). Patterned gene expression directs bipolar planar polarity in Drosophila. Dev. Cell *6*, 343–355.